



## The CLAS12 Central Neutron Detector

P. Chatagnon, J. Bettane, M. Hoballah, G. Hull, M. Imre, D. Marchand, B. Mathon, G. Murdoch, P. Naidoo, S. Niccolai, et al.

### ► To cite this version:

P. Chatagnon, J. Bettane, M. Hoballah, G. Hull, M. Imre, et al.. The CLAS12 Central Neutron Detector. Nuclear Instruments and Methods in Physics Research Section A: Accelerators, Spectrometers, Detectors and Associated Equipment, Elsevier, 2020, 959, pp.163441. 10.1016/j.nima.2020.163441 . hal-02475245

HAL Id: hal-02475245

<https://hal.archives-ouvertes.fr/hal-02475245>

Submitted on 23 Dec 2020

**HAL** is a multi-disciplinary open access archive for the deposit and dissemination of scientific research documents, whether they are published or not. The documents may come from teaching and research institutions in France or abroad, or from public or private research centers.

L'archive ouverte pluridisciplinaire **HAL**, est destinée au dépôt et à la diffusion de documents scientifiques de niveau recherche, publiés ou non, émanant des établissements d'enseignement et de recherche français ou étrangers, des laboratoires publics ou privés.

Elsevier Editorial System(tm) for NIMA  
Proceedings  
Manuscript Draft

Manuscript Number:

Title: The CLAS12 Central Neutron Detector

Article Type: VSI: The CLAS12 Spectrometer

Keywords: Neutron detector; Plastic scintillator; Light collection; Time resolution; Time-of-flight; CLAS12

Corresponding Author: Mr. Pierre Chatagnon,

Corresponding Author's Institution:

First Author: Pierre Chatagnon

Order of Authors: Pierre Chatagnon; Julien Bettane; Mostafa Hoballah; Giulia Hull; Miktat Imre; Dominique Marchand; Bernard Mathon; Gavin Murdoch; Paul Naidoo; Silvia Niccolai; Katheryne Price; Daria Sokhan; Rong Wang

Abstract: The Central Neutron Detector is a scintillator barrel that was designed to detect 0.2-1 GeV neutrons at lab polar angles from 40° to 120° in the CLAS12 spectrometer in Hall~B at Jefferson Laboratory. The design is based on three radial layers of paddles read out at the upstream end of the barrel by photomultipliers tubes. Neighboring paddles in each layer are coupled together at the downstream end of the barrel by "U-turn" light guides. The components of this detector are presented and the performance of the detector with the first beam data taken by CLAS12 is reported.

Dear NIM editors,

The attached manuscript is entitled "The CLAS12 Central Neutron Detector" with lead author Pierre Chatagnon of IPN Orsay. This manuscript is intended to be part of the CLAS12 Spectrometer special NIM issue.

Sincerely,  
Pierre Chatagnon

# The CLAS12 Central Neutron Detector

P. Chatagnon<sup>a</sup>, J. Bettane<sup>a</sup>, M. Hoballah<sup>a</sup>, G. Hull<sup>a</sup>, M. Imre<sup>a</sup>, D. Marchand<sup>a</sup>, B. Mathon<sup>a</sup>, G. Murdoch<sup>b</sup>, P. Naidoo<sup>b</sup>, S. Niccolai<sup>a</sup>, K. Price<sup>a</sup>, D. Sokhan<sup>b</sup>, R. Wang<sup>a</sup>

<sup>a</sup>*Institut de Physique Nucléaire, CNRS-IN2P3, Univ. Paris-Sud, Université Paris-Saclay, 91406 Orsay Cedex, France*

<sup>b</sup>*University of Glasgow, Glasgow G12 8QQ, United Kingdom*

## Abstract

The Central Neutron Detector is a scintillator barrel that was designed to detect 0.2-1 GeV neutrons at lab polar angles from 40° to 120° in the CLAS12 spectrometer in Hall B at Jefferson Laboratory. The design is based on three radial layers of paddles read out at the upstream end of the barrel by photomultiplier tubes. Neighboring paddles in each layer are coupled together at the downstream end of the barrel by “U-turn” light guides. The components of this detector are presented and the performance of the detector with the first beam data taken by CLAS12 is reported.

**Keywords:** Neutron detector, Plastic scintillator, Light collection, Time resolution, Time-of-flight, CLAS12

## 1. Overview

The Central Neutron Detector (CND) is the outermost of the subsystems composing the Central Detector of CLAS12 [1]. It consists of a barrel of three layers of scintillators coupled at their downstream ends with U-turn light guides and read out at their upstream ends by photomultiplier tubes (PMTs) connected to the bars via 1-m-long bent light guides to position them in a fringe-field region of the CLAS12 5-T superconducting solenoid. The CND was installed in the CLAS12 solenoid, and subsequently started its data taking, in the fall of 2017. Geant4-based simulations, calibrated with measurements carried out with the CND using cosmic rays muons, showed that the efficiencies obtainable with this detector and its photon-rejection capabilities are sufficient to collect good statistics on the beam-spin asymmetry for the neutron-DVCS reaction over a wide phase space, using the allocated beam time for CLAS12 with a deuterium target [2]. The first beam data collected by CLAS12 on a proton target confirmed the design performance. This detector will also be used in other  $n$ -DVCS experiments [3], and whenever the detection of the recoil neutron may be required ( $N^*$  program, for instance, or for all the deeply-virtual meson production reactions on the neutron).

## 2. Requirements

Measuring Deeply Virtual Compton Scattering (DVCS) on a neutron target ( $en \rightarrow e'n'\gamma$ ) is one of

the necessary steps to complete our understanding of the structure of the nucleon in terms of Generalized Parton Distributions (GPDs) [4, 5, 6]. DVCS on a neutron target allows one to perform a quark-flavor decomposition of the GPDs when combined with the results for DVCS on a proton target. Moreover, it plays a complementary role to DVCS on a transversely polarized proton target in the determination of the GPD  $E$ , the least known and least constrained GPD that enters Ji’s sum rule [5], which links integrals of GPDs to the total angular momentum of the quarks. To measure  $n$ -DVCS on a deuterium target ( $ed \rightarrow e'n'\gamma(p)$ ) with CLAS12, the electron and the DVCS photon, emitted mainly at small angles, can be detected in the CLAS12 forward calorimeters (ECAL [7] and FT [8]), while the neutron is emitted predominantly (for ~80% of the events) at  $\theta > 40^\circ$  in the laboratory frame, with an average momentum around 0.5 GeV. These kinematic constraint conditions drive the design specifications for the CND. With the aid of the CLAS12 fast Monte Carlo tool (FASTMC), the requirements in terms of angular and momentum resolutions on the detected neutrons were determined by studying the missing mass ( $MM$ ) of the  $e'n'\gamma$  system. Using realistic resolutions on the electron and photon calculated by FASTMC, it was found that if the neutron momentum resolution is kept below 10%, its effect on the  $MM$  resolution is negligible with respect to the other particles in the reaction [9].

Therefore, considering that the detection capabilities of CLAS12 for electrons and high-energy photons are

59 fixed, the requirements of the CND are:

- good neutron identification capabilities for the kinematic range of interest ( $0.2 < p_n < 1.2$  GeV,  $40^\circ < \theta_n < 80^\circ$ );
- neutron momentum resolution  $\sigma_p/p$  within 10%.

#### 64 2.1. Constraints

65 The available radial space in the CLAS12 Central Detector is limited by the presence of the Central Time-of-Flight system (CTOF) [10] and of the solenoid magnet [11], which left about 10 cm free. However, the 3-cm-thick CTOF counters can also be used to detect neutrons, adding an additional 2-3% of detection efficiency. The Central Vertex Tracker (CVT) [12, 13] can be used as a veto for charged particles. Finally, the strong fringe field of the 5-T magnetic field required careful consideration for the positioning and the type of the CND PMTs.

75 After extensive Geant4 simulations and R&D studies devoted to examine the various options for the CND and its possible photodetectors [9], the final design choice was a barrel of standard plastic scintillator bars of trapezoidal cross section, all with their long sides parallel to the beam direction. This geometry is similar to that of the CTOF [10].

82 As previously stated, one of the two requirements of the CND is good neutron identification capabilities. If the charged particles are vetoed by the central tracker, the only particles remaining from the target that can be misidentified for neutrons are photons. Using plastic scintillators, the most straightforward way to distinguish neutrons from photons is by measuring their time-of-flight (TOF) and comparing the values of  $\beta$ :

$$\beta = \frac{P_L}{TOF \cdot c}, \quad (1)$$

90 where  $c$  is the speed of light and  $P_L$  is flight path of the particle from the target to the scintillator bar. This can be obtained, in our geometry, as

$$P_L = \sqrt{z^2 + r^2}, \quad (2)$$

93 where  $z$  and  $r$  are the hit position along the beam  $z$  axis and in the radial direction, respectively. To obtain  $z$  one must measure the time of the hit at both ends of the scintillator bar:

$$z = \frac{1}{2} \cdot v_{\text{eff}} \cdot (t_L - t_R), \quad (3)$$

97 where  $v_{\text{eff}}$  is the effective velocity of light propagation in the scintillator material. To know  $r$  it is necessary 98 to have reasonably small radial segmentation:  $r$  will be

100 given by the distance between the target and the middle  
101 of the hit paddle.

102 Geant4-based simulations show that to ensure a good  
103 photon/neutron separation for the neutron momentum  
104 range of the  $n$ -DVCS reaction, the CND has to be  
105 equipped with photodetectors ensuring a time resolution  
106 of about 150 ps.

#### 107 3. Design

108 The design of the CND is a barrel, coaxial with the  
109 beamline, made of trapezoidal scintillator bars, read out  
110 via standard PMTs attached to long acrylic light guides.  
111 In order to optimize the light collection by matching the  
112 scintillator surface and the PMT entrance window, the  
113 detector is divided into 48 azimuthal segments and 3  
114 radial layers, for a total of 24 blocks<sup>1</sup>, 144 scintillator  
115 bars, 144 PMTs, and 72 U-turn light guides (see Fig. 1).  
116 The radial thickness of all scintillators is 30 mm. The  
117 other dimensions are listed in Table 1.

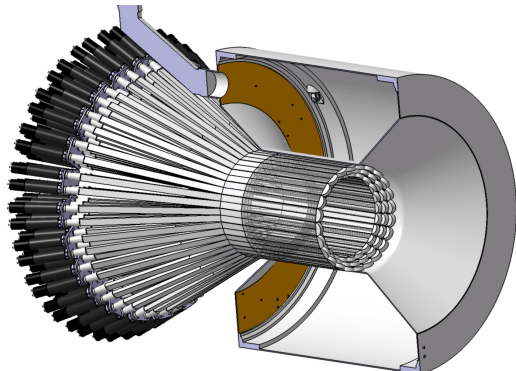


Figure 1: Drawing of the CND inserted in the CLAS12 solenoid, which is shown in a cut-view.

Layer	Inner face width (mm)	Outer face width (mm)	Length (mm)
1	35.92	39.87	665.72
2	40.0	43.95	700.0
3	44.08	48.03	734.28

Table 1: Dimensions (mm) of the trapezoidal scintillator bars of the CND. The layer numbers go from the innermost (1) to the outermost (3). The thickness of all bars is 30 mm.

---

<sup>1</sup>A “block” or “sector” is formed by three radial layers of coupled pairs of scintillator bars.

118 **4. Hardware Components and Construction**

119 Comparative measurements were carried out to  
120 choose the elements composing the CND. The tests  
121 were geared towards optimizing the time resolution,  
122 which is the key parameter to ensure  $n/\gamma$  separation,  
123 and containing all associated costs. Different prototypes  
124 were constructed and employed for measurements of  
125 time resolution and light-yield during cosmic ray test-  
126 ing to optimize the final design choices for scintillator  
127 type, PMT, wrapping material, PMT magnetic shielding  
128 configuration, shape of the U-turn light guide, and glue  
129 for the optical coupling. The outcomes of these tests are  
130 discussed in detail in Ref. [9]. The chosen components  
131 are:

- 132 • 144 EJ-200 scintillator bars, by Eljen Technology;
- 133 • 144 Hamamatsu R10533 2-in PMTs;
- 134 • 72 semi-circular-shaped U-turn light guides of  
135 Polymethyl Methacrylate (PMMA);
- 136 • aluminum foil as reflector material wrapping the  
137 scintillator bars;
- 138 • a 1-mm-thick mu-metal cylinder plus a 5-mm-  
139 thick mild steel cylinder to shield each PMT from  
140 the stray magnetic field of the CLAS12 solenoid;
- 141 • coupling with optical grease between PMT and  
142 light guide;
- 143 • M-Bond200 glue for the junctions between scintil-  
144 lators and light guides.

145 The 24 blocks composing the CND were assembled  
146 in the mechanical shop of IPN Orsay [9] and then  
147 shipped to Jefferson Lab (JLab), along with the com-  
148 ponents of the support structure. The support structure  
149 consists of six separate aluminum arches that are fas-  
150 tened together to form a ring, which is in turn attached  
151 to the solenoid by means of stainless-steel brackets. The  
152 support structure was installed first onto the CLAS12  
153 solenoid, and then the 24 blocks of the CND were in-  
154 serted, one by one, and secured onto the structure. The  
155 PMTs, within their shields, were then connected to the  
156 end of the light guides, to which they were coupled with  
157 optical grease. Figure 2 shows the detector after its in-  
158 stallation.

159 **5. Electronics and Readout**

160 The completely resistive high-voltage dividers of the  
161 CND were designed following the voltage distribution



Figure 2: The CND as installed in the CLAS12 solenoid.

162 ratio suggested by Hamamatsu. The tube-base assembly  
163 was developed at IPN Orsay with the aim to mechani-  
164 cally match the mild-steel PMT shielding, for a com-  
165 pact and robust design. In order to operate the PMTs,  
166 high voltages (typically in the range of 1500 V) are pro-  
167 vided by multi-channel CAEN SY527 power supplies.  
168 The HV boards adopted for the CND are CAEN A734N  
169 (16 channels, 3 kV maximum voltage, 3 mA maximum  
170 current). The signal of each PMT is sent to an active  
171 splitter. The three splitter modules used for the CND  
172 were originally developed by IPN Orsay for the G0 ex-  
173 periment (Hall C, JLab) [14]. Each module is an active  
174 64-channel splitter with unity gain, so that there is no  
175 loss of amplitude. The 64 SMA inputs are placed in the  
176 back panel. In the front panel there are 8 8-channel out-  
177 put connectors (DMCH) for the time signals and 4 16-  
178 channel output connectors (FASTBUS) for the charge  
179 signals. The charge signal from the splitter is sent to  
180 JLab-designed 16-channel 250 MHz VXS-based flash-  
181 ADCs (FADCs). The time signal from the splitter is  
182 sent to a constant fraction discriminator (CFD) GAN-  
183 ELEC FCC8, originally developed for the TAPS detec-  
184 tor in Mainz. Each CFD module is an 8-channel CA-  
185 MAC unit with LEMO 00 input connectors and 2x8-  
186 pin output connectors in differential ECL. The threshold  
187 can be set for each channel individually using a manual  
188 switch or remote control, and no time-walk adjustment

Constant name	Number of constants	Units
$t_{LR}$	72	ns
$v_{eff}$	144	cm/ns
$u_t$	72	ns
$t_{LR_{ad}}$	72	ns
$t_{off}$	72	ns
$A_L$	144	cm
$MIP_D, MIP_T$	144 each	no units

Table 2: The constants computed in the CND calibration. See text for details.

is required for the module. The discriminated time signal then goes to the TDC (CAEN VX1290A, 32 channels/board, 25 ps/channel resolution). In total, the read out system includes 3 splitter modules, 19 CFD modules, 5 TDC boards, and 8 FADC boards.

## 6. Calibration

The calibration of the CND with beam data is done in two steps: the timing calibration, which allows us to obtain effective velocities and time offsets, which are, in turn, necessary to deduce timing and position information of the hits; and the energy calibration, in which attenuation lengths and energy conversion factors are extracted. Table 2 summarizes the calibration constants necessary to reconstruct CND hits.

### 6.1. Timing Calibration

There are five calibration constants that must be determined as part of the CND timing calibration: the two left-right time offsets ( $t_{LR}$  and  $t_{LR_{ad}}$ ), the effective velocity ( $v_{eff}$ ), the propagation time in the U-turn ( $u_t$ ), and the global time offset with respect to the event start time ( $t_{off}$ ). The calibrations of these constants must be done in the following order:  $t_{LR}$ ,  $v_{eff}$ ,  $u_t$ ,  $t_{LR_{ad}}$ , and finally  $t_{off}$ . Each of these constants is determined using charged particles from beam interactions in the target.

The raw hit times  $t_{LR}$  are obtained from the measured TDC channel using a slope constant of 0.0234 ns/channel for all channels.

The paddle in which the hit occurs must be determined before the calibration procedure can be applied. The left and right times of a hit in the left paddle (we label them as  $t_{LL}$  and  $t_{RL}$  where the first index corresponds to the paddle under examination, while the second indicates the paddle in which the primary hit happened) are given by:

$$t_{LL} = t_{off} + t_{t_{off}} + \frac{z}{v_{eff_L}} + t_S + TDC_j, \quad (4)$$

$$t_{RL} = t_{off} + t_{t_{off}} - \frac{z}{v_{eff_L}} + \frac{L}{v_{eff_L}} + \frac{L}{v_{eff_R}} + u_t + t_S + t_{off_R} - t_{off_L} + TDC_j, \quad (5)$$

where  $t_{t_{off}}$  is the time of flight extracted using the CVT [12, 13] path length information,  $z$  is the position of the hit measured from the upstream end of the paddle,  $L$  is the length of the paddle,  $t_S$  is the start time of the event,  $t_{off_L}$  and  $t_{off_R}$  are time offsets associated with the left and right coupled paddle, and  $TDC_j$  is the TDC clock jitter. Similarly if the hit happened in the right paddle one can write:

$$t_{LR} = t_{off} + t_{t_{off}} - \frac{z}{v_{eff_R}} + \frac{L}{v_{eff_L}} + \frac{L}{v_{eff_R}} + u_t + t_S + TDC_j, \quad (6)$$

$$t_{RR} = t_{off} + t_{t_{off}} + \frac{z}{v_{eff_R}} + t_S + t_{off_R} - t_{off_L} + TDC_j. \quad (7)$$

Defining  $\Delta$  and  $\Delta'$  as:

$$\Delta = \frac{L}{v_{eff_L}} - \frac{L}{v_{eff_R}}, \quad (8)$$

$$\Delta' = t_{RX} - t_{LR} + t_{off_R} - t_{off_L}, \quad (9)$$

where the index X can be R or L, one can compute  $\Delta' - \Delta$  for both cases (hit in the left paddle or hit in the right paddle). If the hit is in the left paddle:

$$\Delta' - \Delta = \frac{2z}{v_{eff_L}} - \frac{2L}{v_{eff_L}} - u_t < 0. \quad (10)$$

If the hit is in the right paddle:

$$\Delta' - \Delta = \frac{2L}{v_{eff_R}} - \frac{2z}{v_{eff_R}} + u_t > 0. \quad (11)$$

If  $\Delta' < \Delta$ , the paddle in which the hit happened is the left one, otherwise it is the right one. This procedure to determine the hit paddle depends on constants yet to be calibrated ( $v_{eff}$  and  $t_{off_R} - t_{off_L}$ ). Therefore, at least two iterations of the calibrations of  $v_{eff}$  and  $t_{off_R} - t_{off_L}$  are required.

#### 6.1.1. Left-Right Timing Offset

The left-right time offset refers to the time misalignment between two coupled paddles. It is determined in two steps. The first step relies on the U-turn structure of the CND to extract an estimate of this offset  $t_{LR}$ . The second step corrects  $t_{LR}$  to obtain the *adjusted* value  $t_{LR_{ad}}$  by taking into account the effective velocities of both coupled paddles. There is one value of  $t_{LR}$  and  $t_{LR_{ad}}$  for each pair of coupled paddles.

231 There are two different algorithms to find  $t_{LR}$  depending  
 232 on whether the data were taken with or without magnetic field of the solenoid.  
 233

- 234 • If the solenoid field is off, the U-turn light guide  
 235 coupling two adjacent CND paddles induces a gap  
 236 in the time difference  $t_R - t_L$  plots. The  $t_{LR}$  constant  
 237 is defined as the time difference value at the center  
 238 of the gap.
- 239 • If the solenoid is on, “double hits” occur. When the  
 240 trajectory of a charged particle bent in the solenoid  
 241 field crosses two adjacent coupled paddles, the two  
 242 L/R signals have very similar TDC values (see  
 243 Fig. 3). Such hits induce a peak instead of a gap  
 244 in the time difference plots (see Fig. 4).  $t_{LR}$  is de-  
 fined as the position of this peak.

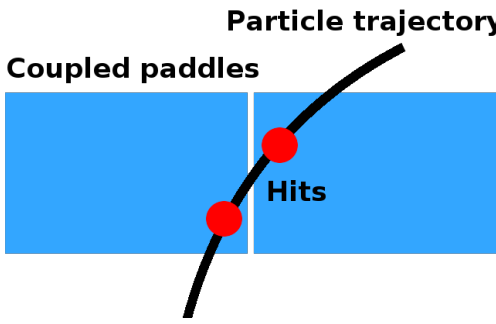


Figure 3: Double hits in the CND produced by the curved trajectory of a charged particle in the solenoid field. Both hits have similar TDC values, resulting in a peak in the time difference distribution.

246 The “field on” case is illustrated in Fig. 4. Typical val-  
 247 ues for the offsets are below 5 ns.  $t_{LR}$  is not used in the  
 248 reconstruction, but it is nonetheless necessary to remove  
 249 double hits from the subsequent calibration steps.  $t_{LR_{ad}}$ ,  
 250 defined below, is used in the reconstruction. Once  $t_{LR}$   
 251 constants have been determined, they are corrected to  
 252 account for the different effective velocities of the two  
 253 coupled paddles.

For hits in the left paddle, the two associated TDCs can be expressed with Eqs. 6 and 7.  $t_{LR_{ad}}$  is defined as:

$$t_{LR_{ad}} = t_{off_R} - t_{off_L}. \quad (12)$$

Then one can write:

$$\frac{t_{LL} - t_{RL}}{2} = \frac{z}{v_{eff_L}} - C_L, \quad (13)$$

where  $C_L$  is the negative of the intercept of  $\frac{t_L - t_R}{2}$  vs.  $z$ ,  $C_L$  and is given by:

$$C_L = \frac{L}{2 \cdot v_{eff_L}} + \frac{L}{2 \cdot v_{eff_R}} + \frac{u_t}{2} + \frac{t_{LR_{ad}}}{2}. \quad (14)$$

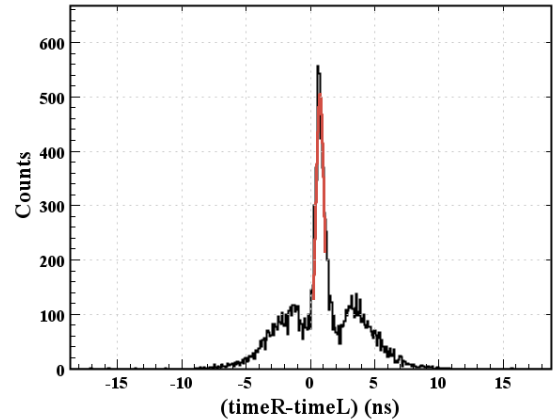


Figure 4: Left-right time difference for data with the solenoid field on: double hits, with equal TDC values, produce a peak instead of a gap.

For hits in the right paddle, the corresponding intercept  $C_R$  is given by:

$$C_R = \frac{L}{2 \cdot v_{eff_R}} + \frac{L}{2 \cdot v_{eff_L}} + \frac{u_t}{2} - \frac{t_{LR_{ad}}}{2}. \quad (15)$$

Combining Eqs. 14 and 15,  $t_{LR_{ad}}$  is given by:

$$t_{LR_{ad}} = C_L - C_R. \quad (16)$$

#### 6.1.2. Effective Velocity

The effective velocity  $v_{eff}$  is the speed of the light in the scintillators and the light guides. There is one  $v_{eff}$  value for each coupled paddle.  $v_{eff}$  is obtained from the following equation:

$$z = (t_L - t_R) \cdot \frac{v_{eff}}{2} + c, \quad (17)$$

where  $z$  is the  $z$  position of the hit in the CND with respect to the upstream end of the CND paddles and  $c$  is an unknown constant.  $z$  is obtained independently from the CND, using the CVT. The above equation is true for hits in the left paddles. For hits in the right paddles, the sign of the time difference must be changed.  $v_{eff}$  is extracted by fitting the  $\frac{t_R - t_L}{2}$  vs.  $z$  distribution as shown in Fig. 5. For each slice in  $z$ , the position of the maximum from a Gaussian fit is plotted against  $z$ . The slope of the obtained distribution gives  $v_{eff}$ . The expected values for  $v_{eff}$  are around 16 cm/ns.

#### 6.1.3. U-turn Propagation Time

The U-turn propagation time  $u_t$  is the time spent for the light to travel through the U-turn light guide. It is

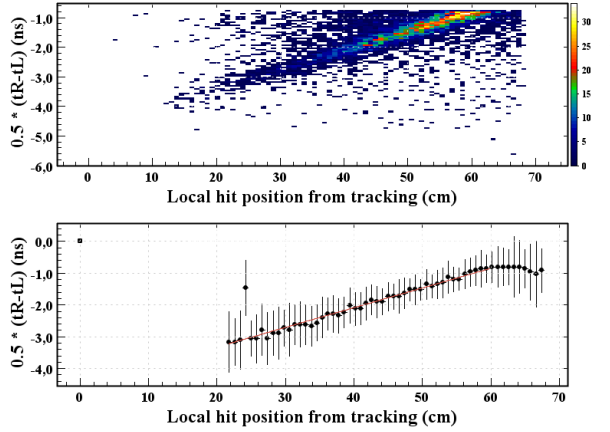


Figure 5: Plots used to determine the effective velocity for a CND paddle. The top plot shows the raw  $\frac{t_R - t_L}{2}$  vs.  $z$  and the bottom plot is the distribution showing the linear fit.

used as a time offset on the indirect signal in the time and position reconstruction. There is one  $u_t$  value for each pair of paddles. The algorithm to extract  $u_t$  is very similar to the one used in the  $v_{\text{eff}}$  procedure: the intercept of the  $\frac{t_R - t_L}{2}$  vs.  $z$  distribution (see Fig. 5) is extracted for both coupled paddles to determine  $u_t$ .

From the sum of the intercepts  $C_L$  in Eq. 15 and  $C_R$  in Eq. 15,  $u_t$  is obtained as :

$$u_t = C_R + C_L - L \left( \frac{1}{v_{\text{eff}_R}} + \frac{1}{v_{\text{eff}_L}} \right). \quad (18)$$

The values for  $u_t$  are typically in the range from 0.5 ns - 1.5 ns, with layer 1 values around 0.6 ns, layer 2 around 1 ns, and layer 3 around 1.4 ns.

#### 6.1.4. Global Time Offset

The global time offset  $t_{\text{off}}$  refers to the time difference between the start time value and the vertex time computed from the CND hit time and the CVT path length information. There is one  $t_{\text{off}}$  value for each pair of coupled paddles.  $t_{\text{off}}$  is given by:

$$t_{\text{off}} = \frac{t_L + t_R}{2} - t_S - t_{\text{tof}} - \frac{L}{2} \cdot \left( \frac{1}{v_{\text{eff}_R}} + \frac{1}{v_{\text{eff}_L}} \right) - \frac{u_t}{2} - \frac{t_{\text{LR}_{\text{ad}}}}{2} - \text{TDC}_j, \quad (19)$$

where  $t_{\text{tof}}$  is calculated using CVT information assuming the particles are pions. For this, a negative charge is required, as most of the negative particles in the Central Detector are pions. The position of the peak of the above distribution gives  $t_{\text{off}}$  (see Fig. 6). These values depend mainly on the start time  $t_S$ , which is calculated using the CLAS12 Forward Time-of-Flight Sys-

tem (FTOF) [15]. The variations of  $t_{\text{off}}$  between different pairs of paddles are typically below 10 ns.

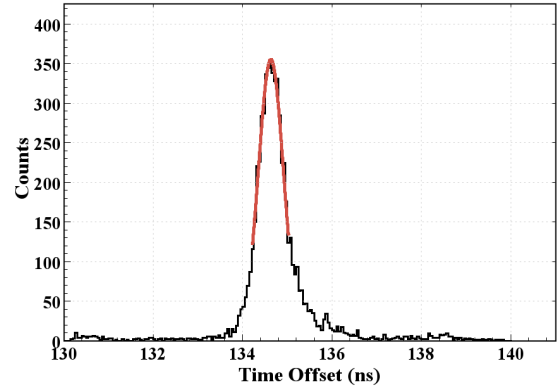


Figure 6: Plot used to determine the global time offset. The distribution is fit with a Gaussian and the position the peak corresponds to  $t_{\text{off}}$ .

## 6.2. Energy Calibration

There are three calibration constants for the energy determination in each paddle of the CND: the attenuation length ( $A_L$ ), the ADC-to-energy constants for direct minimum-ionizing particles (MIPs) ( $MIP_D$ ), and the ADC-to-energy constants for indirect MIPs ( $MIP_I$ ). These three calibration steps can be performed almost independently from the timing calibration, however,  $t_{\text{LR}_{\text{ad}}}$  is needed to determine if an ADC signal is direct or indirect (i.e. the hit happened in the considered paddle or in its coupled partner).

### 6.2.1. Attenuation Length

The attenuation length  $A_L$  accounts for the light attenuation along the length of the scintillators and light guides. There is an  $A_L$  value for each paddle. For hits in the left paddle, the two associated ADCs can be written as:

$$ADC_L = \frac{E}{E_0} \cdot MIP_D \cdot e^{\frac{-z}{A_L}}, \quad (20)$$

$$ADC_R = \frac{E}{E_0} \cdot MIP_I \cdot e^{\frac{-z(L-z)}{A_L}}, \quad (21)$$

where  $MIP_D$  and  $MIP_I$  are constants defined in the Section 6.2.2 ( $MIP_I$  includes the effect of the light attenuation in the  $R$  paddle),  $E$  is half the energy deposited by the particle in the scintillator, and  $E_0$  is half the energy deposited by a MIP in the scintillators.  $E_0$  is given by:

$$E_0 = \frac{h \cdot 2.001}{2} \text{ MeV}, \quad (22)$$

where  $h$  is the thickness of each scintillator. All the above equations are valid for hits in the left paddles, while for hits in the right paddles, the corresponding equations are obtained by switching the  $L/R$  indices. From Eqs. 20 and 21 the following relation is derived:

$$\ln(ADC_L/ADC_R) = c - \frac{2 \cdot z}{A_L}, \quad (23)$$

where  $c$  is a constant depending on  $MIP_D$ ,  $MIP_I$ , and  $L$ .  $A_L$  is given by the slope of the distribution in Eq. 23 as shown in Fig. 7. Values for  $A_L$  are typically around 150 cm.

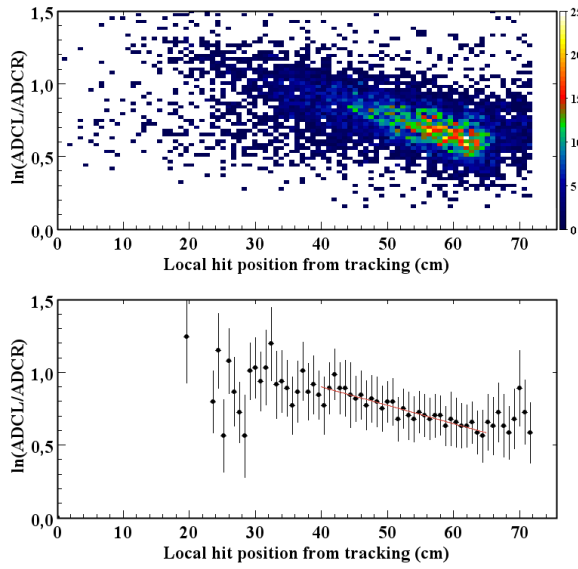


Figure 7: Plots used to determine  $A_L$ . The top plot shows the raw  $\ln(ADC_L/ADC_R)$  vs.  $z$  distribution for one pair of paddles. Slices in  $z$  are fit with a Gaussian and the mean is the plotted against  $z$ . The corresponding distribution and its associated linear fit is shown in the bottom plot.

#### 6.2.2. Energy Calibration Parameters

The final step of the calibration of the CND is the determination of the energy conversion parameters  $MIP_D$  and  $MIP_I$ . There are two energy parameters for each paddle, thus there are four energy parameters for each pair of coupled paddles, denoted as  $MIP_{DL}$ ,  $MIP_{IL}$ ,  $MIP_{DR}$ ,  $MIP_{IR}$ .

In the following, we only consider a hit in the left paddle. Equations for hits in right paddles are obtained by switching the  $L/R$  indices. For hits in the left paddle, only  $MIP_{DL}$  and  $MIP_{IL}$  can be obtained. In the following they are referred to as  $MIP_D$  and  $MIP_I$ . From

Eqs. 20 and 21, one gets:

$$\ln\left(\frac{ADC_L}{ADC_R}\right) = \ln\left(\frac{MIP_D}{MIP_I}\right) + \frac{L}{A_L} - \frac{2 \cdot z}{A_L} \quad (24)$$

$$\sqrt{ADC_L \cdot ADC_R} = \frac{E}{E_0} \cdot \sqrt{MIP_D \cdot MIP_I} e^{-\frac{L}{2A_L}}. \quad (25)$$

From Eq. 24, the intercept of the  $\ln\left(\frac{ADC_L}{ADC_R}\right)$  vs.  $z$  distribution (Fig. 7) gives the ratio  $\frac{MIP_D}{MIP_I}$ . The product  $MIP_D \cdot MIP_I$  is obtained using Eq. 25 after filtering MIPs and correcting for the path traveled by the MIP in the scintillators. Indeed for MIPs,  $E$  can be written as:

$$E = \frac{\text{path}}{h} \cdot E_0, \quad (26)$$

where *path* is the path length traveled by the MIP in the scintillator, which is obtained using the CVT tracking information by extrapolating the particle trajectory at the radius of the CND hit. Selecting MIPs and correcting for the path length removes the energy dependence from Eq. 25, which becomes:

$$\sqrt{ADC_L \cdot ADC_R} = \frac{\text{path}}{h} \cdot \sqrt{MIP_D \cdot MIP_I} e^{-\frac{L}{2A_L}}. \quad (27)$$

The distribution of  $\sqrt{ADC_L \cdot ADC_R} \cdot \frac{h}{\text{path}}$  is fit with a Landau function and the position of the peak  $p$  is extracted as shown in Fig. 8.  $MIP_D$  and  $MIP_I$  are given by:

$$MIP_D = \sqrt{e^{-(i-\frac{L}{A_L})} \cdot e^{\frac{L}{A_L}} \cdot p^2}, \quad (28)$$

$$MIP_I = \sqrt{e^{-(i-\frac{L}{A_L})} \cdot e^{\frac{L}{A_L}} \cdot p^2}, \quad (29)$$

where  $i$  and  $p$  are the intercept and peak position defined above.  $MIP_D$  and  $MIP_I$  are typically around 2000 and 500, respectively.

## 7. Simulation

In order to study the performance of the CND, its geometry and response were included in the CLAS12 Geant4-based simulation package, GEMC [16]. The Barks effect, for which the number of optical photons produced for a given energy deposition in the scintillator depends on the particle type, and the hit digitization for the CND, were introduced in GEMC. The timing resolution and the energy loss due to the U-turn geometry were included in the simulation using the values measured in the cosmic-ray tests. Details on the digitization

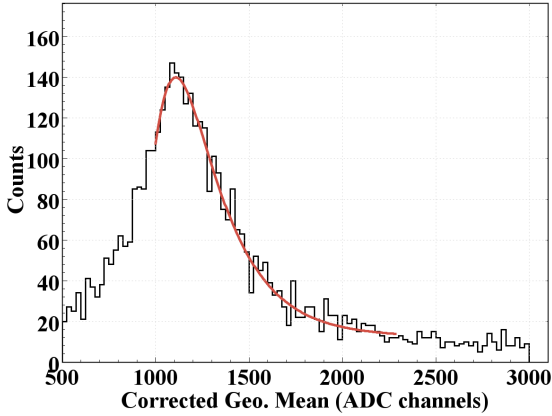


Figure 8:  $\sqrt{ADC_L \cdot ADC_R} \cdot \frac{h}{path}$  distribution fit with a Landau function. The events in this plot are identified as MIPs by requiring a pion. The particle identification is performed requiring a negative charge, as most negatively charged particles in the Central Detector are pions.

and on the hit and event reconstruction are explained in Ref. [16] and Ref. [17], respectively.

Simulations of the  $n$ -DVCS reaction were run to evaluate the efficiency of the CND for neutrons and its angular and momentum resolutions. Figure 9 shows the neu-

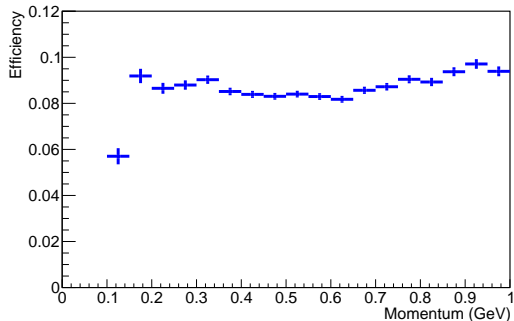


Figure 9: Simulation results for the efficiency for the detection of neutrons in the CND from the  $n$ -DVCS reaction.

tron detection efficiency as a function of neutron momentum. It is fairly constant and has an average value of roughly 9%. The angular resolution  $\sigma_\theta$ , obtained via Gaussian fits of the difference between the generated and reconstructed  $\theta$ , is also fairly constant as a function of neutron momentum, with an average value of about  $2.5^\circ$ . The resolution on the azimuthal angle is directly connected to the total number of scintillator bars along  $\phi$  with the angular size of each bar  $\Delta\phi = 7.5^\circ$ ,  $\sigma_\phi$  is given by  $\Delta\phi/2 = 3.75^\circ$ . The resolution on the neutron

momentum, which is obtained knowing  $\beta$  and having performed the particle identification, according to the formula

$$p = \frac{\beta \cdot m_n}{\sqrt{1 - \beta^2}}, \quad (30)$$

is also strictly connected to the time resolution. The average relative momentum resolution  $\sigma_p/p$  is  $\sim 8\%$ . No appreciable variation of momentum resolution was observed as a function of the neutron polar angle.

Since the charged particles passing through the CND will be vetoed by the CVT, the only particles that could be mistaken for neutrons in the CND are photons. The efficiency of the CND for photons has been estimated by simulations, and it is slightly larger than for neutrons (on the order of 15%, having little energy dependence). Neutrons can be discriminated from photons by means of their  $\beta$ . Therefore, the  $\beta$  distributions that can be obtained with the CND for neutrons and photons were studied with the help of the GEMC simulation. Neutrons and photons of momenta varying between 0.1 and 1 GeV were generated at a fixed azimuthal angle ( $\phi = 3.75^\circ$ ). Figure 10 shows the comparison between the  $\beta$  distributions obtained for neutrons of various momenta (0.2, 0.4, 0.7, and 1 GeV) and for 1-GeV photons. All particles in this plot were emitted at  $\theta = 60^\circ$ . A small portion of the neutrons having momentum of 1 GeV can be taken as photons, as their  $\beta$  distributions begin to overlap, while the  $n/\gamma$  separation is clear for lower momenta — which corresponds to most of the range of interest for  $n$ -DVCS, as only about 8% of the events are expected to have  $p_n > 0.9$  GeV.

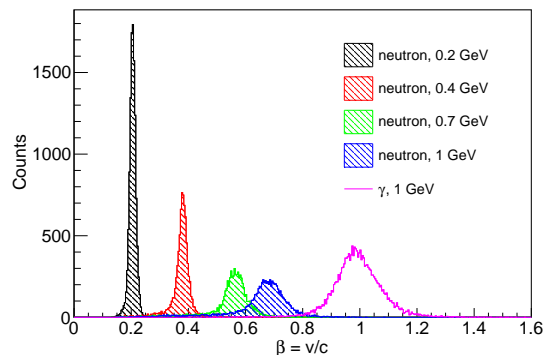


Figure 10: Simulation results for the  $\beta$  distributions for neutrons with  $p_n = 0.2$  GeV (black),  $p_n = 0.4$  GeV (red),  $p_n = 0.7$  GeV (green),  $p_n = 1$  GeV (blue), and photons with  $E = 1$  GeV (purple). The threshold on the deposited energy is 3 MeV. The plot shows all reconstructed particles integrated over  $\phi$ . Equal neutron and photon yields were assumed.

369 **8. Performance**

370 After the calibration constants are determined, the  
 371 timing, position, and deposited energy of each hit are  
 372 reconstructed, and clusters are formed grouping hits ac-  
 373 cording to their position and timing [17].

374 Data taken during the first CLAS12 experiments on  
 375 hydrogen and deuterium targets, and with various beam  
 376 energies (7.5 and 10.6 GeV), were analyzed to verify  
 377 the performance of the CND.

The timing performance for the three layers of the CND is illustrated in Fig. 11, showing the vertex time difference  $v_t$  for selected negative tracks, assumed to be all pions, integrated over all sectors defined as

$$v_t = t_{\text{CND}} - (t_s - v_{z,\text{corr}}) - \frac{P_L}{c \cdot \beta}, \quad (31)$$

where  $t_{\text{CND}}$  is the mean time reconstructed from the L and R paddles,  $t_s$  is the event start time determined by the RF bucket matched with the FTOF vertex time,  $v_{z,\text{corr}}$  accounts for the actual  $z$  position of the interaction vertex,  $P_L$  is the path length from the event vertex to the CND, and

$$\beta = \frac{p}{\sqrt{p^2 + m^2}}, \quad (32)$$

with  $p$  the momentum measured by the CVT, and  $m$  the pion mass. The distribution of  $v_t$  is centered at 0. From the width of the  $v_t$  distribution the timing resolution of each CND paddle convoluted with the CVT resolution can be determined as:

$$\sigma_t = \sqrt{\sigma_{v_t}^2 - \sigma_{t_s}^2} = 185 \text{ ps}, \quad (33)$$

378 assuming the resolution of the start time  $\sigma_{t_s} = 20 \text{ ps}$  [15].  
 379 The timing resolution for the 144 individual CND coun-  
 380 ters is shown in Fig. 12. Its average (indicated by the  
 381 horizontal line) is around 185 ps, which is more than  
 382 the average 148 ps intrinsic timing resolution measured  
 383 with cosmic rays [9]. This discrepancy is due to mul-  
 384 tiple factors, such as the current, not fully optimized,  
 385 quality of the calibrations and reconstruction, as well as  
 386 the uncertainty of the path length and on the other non-  
 387 CND contributions to Eq. 31.

388 The position reconstruction performance of the CND  
 389 is shown in Fig. 13, which displays the difference be-  
 390 tween the  $z$  coordinate (along the beamline) computed  
 391 by the CND and by the CVT for negative tracks in all  
 392 three layers of the CND integrated over all paddles.  
 393 Its Gaussian width is  $\sim 3 \text{ cm}$ , corresponding roughly to  
 394  $4^\circ$  in polar-angle resolution. This corresponds to the  
 395 convolution of the angular resolutions of the CND and  
 396 CVT.

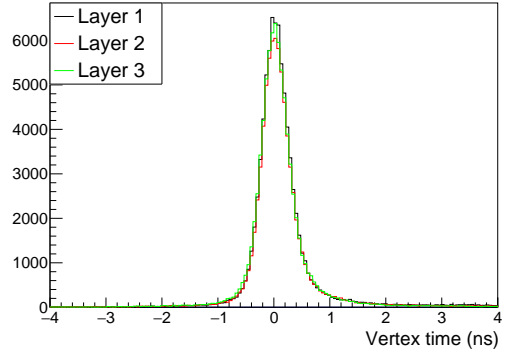


Figure 11: Difference between the vertex time computed combining CND and CVT information with the start time computed by the FTOF for negative tracks in all the three layers of the CND integrated over all paddles.

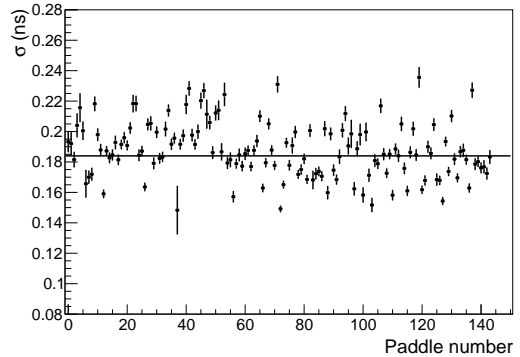


Figure 12: Timing resolution for each CND counter convoluted with the CVT resolution.

397 Figure 14 shows the energy deposited divided by path  
 398 length for selected MIPs. It peaks at around the ex-  
 399 pected value of 2.001 MeV/cm.

400 **8.1. Neutron Detection Efficiency**

401 The exclusive reaction  $e p \rightarrow e' n \pi^+$  was analyzed to  
 402 evaluate the neutron detection efficiency of the CND.  
 403 The data used were taken with a 7.5-GeV electron beam  
 404 incident on a liquid-hydrogen target. Events with an  
 405 electron and a  $\pi^+$  in the CLAS12 Forward Detector were  
 406 selected. The missing mass of the  $e' \pi^+ X$  system is plot-  
 407 ted versus  $\beta_X$  in Fig. 15. The missing particle is re-  
 408 quired to be in the CLAS12 Central Detector ( $\theta > 40^\circ$ ).  
 409 The effect of this selection is shown in Fig. 15. We  
 410 apply an additional cut on  $\beta$  of the missing neutron

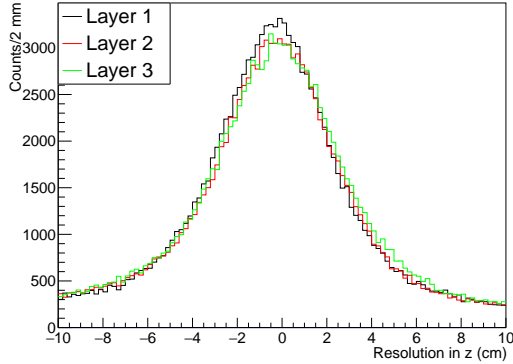


Figure 13: Difference between the  $z$  coordinate (along the beamline) computed by the CND and the CVT, for negative tracks in all three CND layers integrated over all paddles.

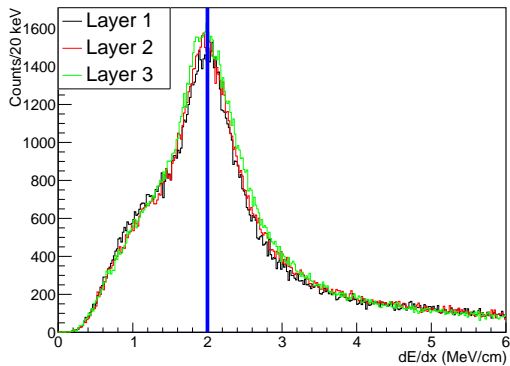


Figure 14:  $dE/dx$  for MIPs in the three layers of the CND integrated over all sectors. The blue line indicates the nominal value for the expected energy deposit of a MIP in a centimeter of plastic scintillator.

(0.2 <  $\beta_X$  < 0.8). From this set of  $ep \rightarrow e'(n)\pi^+$  events, events with a neutron identified by the CND (CND cluster with  $E_{dep} > 2.5$  MeV, no associated CVT tracks,  $\beta < 0.8$ ) were selected. If multiple neutron candidates were detected by the CND, the neutron with the smallest momentum separation from the missing neutron was kept. A cut on  $\beta > 0.2$  was applied to remove out-of-time hits that could be mistaken as neutrons. Finally, the detected neutron and the missing neutron azimuthal angle difference is constrained to be less than 20°.

The efficiency was measured in bins of missing neutron polar angle and as a function of missing momentum. For each bin in polar angle and momentum, the efficiency is defined as the ratio of events with a detected neutron to the number of missing neutron events.

The result is shown in Fig. 16. The detection efficiency extracted from this method is consistent with simulation predictions and with the design specifications of the CND.

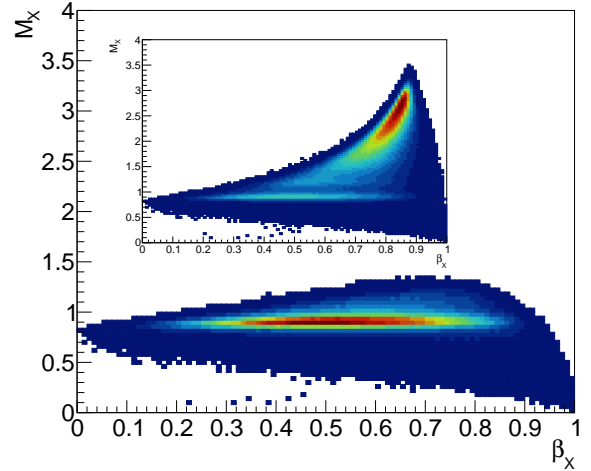


Figure 15: Missing mass  $M_X$  versus  $\beta_X$  of the  $ep \rightarrow e'\pi^+X$  reaction. The outer plot shows the effect of selecting events where the missing particle  $X$  is emitted in the CLAS12 Central Detector.

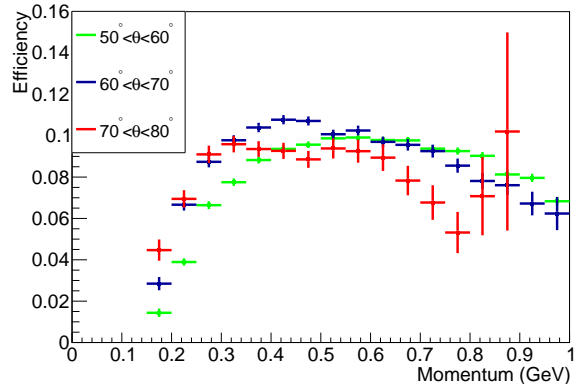


Figure 16: Neutron detection efficiency of the CND as a function of momentum for three bins in polar angle.

## 9. Conclusions

This article presents the requirements, the design, the calibration and reconstruction procedures, and the performance of the Central Neutron Detector for CLAS12. It consists of a barrel of three layers of scintillators

435 coupled at their downstream ends with U-turn light  
 436 guides and read out at their upstream ends by conven-  
 437 tional PMTs connected to the bars via 1-m-long bent  
 438 light guides and placed in the fringe field region of  
 439 the CLAS12 solenoid. The performance measured with  
 440 beam data, which agree with the results of our Geant4-  
 441 based simulations, show that the efficiencies obtainable  
 442 with this detector and its photon-rejection capabilities  
 443 allow for the collection of good statistics on the beam-  
 444 spin asymmetry for the  $n$ -DVCS reaction over a wide  
 445 phase space, using the allocated beam time for CLAS12  
 446 with a deuterium target [2]. This detector will also be  
 447 used in other  $n$ -DVCS experiments [3], and whenever  
 448 the detection of the recoil neutron may be required (e.g.  
 449 the excited nucleon  $N^*$  program or all of the deeply virtual  
 450 meson production reactions on the neutron).

## 451 10. Acknowledgments

452 This work was supported by IN2P3-CNRS (France)  
 453 and European (Sixth Framework Program I3-HP) funds.  
 454 This material is also based upon work supported by the  
 455 U.S. Department of Energy, Office of Science, Office of  
 456 Nuclear Physics under contract DE-AC05-06OR23177.

- 457 [1] V. D. Burkert, et al., The CLAS12 Spectrometer at Jefferson  
 458 Laboratory, to be published in Nucl. Inst. and Meth. A, (2020)  
 459 (see this issue).
- 460 [2] S. Niccolai, et al., Deeply virtual Compton scattering on the neu-  
 461 tron with CLAS12 at 11 GeV, Jefferson Lab experiment E12-11-  
 462 003.
- 463 [3] S. Niccolai, et al., Deeply virtual Compton scattering on the neu-  
 464 tron with a longitudinally polarized deuteron target, Jefferson  
 465 Lab experiment E12-06-109a.
- 466 [4] D. Muller, D. Robaschik, B. Geyer, F. M. Dittes, J. Hore-  
 467 josi, Wave functions, evolution equations and evolution ker-  
 468 nels from light ray operators of QCD, Fortsch. Phys. 42 (1994)  
 469 101–141. [arXiv:hep-ph/9812448](https://arxiv.org/abs/hep-ph/9812448), doi:10.1002/prop.  
 470 2190420202.
- 471 [5] X.-D. Ji, Gauge-Invariant Decomposition of Nucleon Spin,  
 472 Phys. Rev. Lett. 78 (1997) 610–613. [arXiv:hep-ph/9603249](https://arxiv.org/abs/hep-ph/9603249),  
 473 doi:10.1103/PhysRevLett.78.610.
- 474 [6] A. V. Radyushkin, Scaling limit of deeply virtual Compton scat-  
 475 tering, Phys. Lett. B380 (1996) 417–425. [arXiv:hep-ph/  
 476 9604317](https://arxiv.org/abs/hep-ph/9604317), doi:10.1016/0370-2693(96)00528-X.
- 477 [7] G. Asryan, et al., The CLAS12 Forward Electromagnetic  
 478 Calorimeter, to be published in Nucl. Inst. and Meth. A, (2020)  
 479 (see this issue).
- 480 [8] A. Acker, et al., The CLAS12 Forward Tagger, to be published  
 481 in Nucl. Inst. and Meth. A, (2020) (see this issue).
- 482 [9] S. Niccolai, et al., The central neutron detector for CLAS12,  
 483 Nucl. Instrum. Meth. A904 (2018) 81–92. doi:10.1016/j.  
 484 nima.2018.07.029.
- 485 [10] D. S. Carman, et al., The CLAS12 Central Time-of-Flight Sys-  
 486 tem, to be published in Nucl. Inst. and Meth. A, (2020) (see this  
 487 issue).
- 488 [11] R. Fair, et al., The CLAS12 Superconducting Magnets, to be  
 489 published in Nucl. Inst. and Meth. A, (2020) (see this issue).
- 490 [12] M. A. Antonioli, et al., The CLAS12 Silicon Vertex Tracker, to  
 491 be published in Nucl. Inst. and Meth. A, (2020) (see this issue).

- [13] A. Acker, et al., The CLAS12 MicroMegas Tracker, to be pub-  
 492 lished in Nucl. Inst. and Meth. A, (2020) (see this issue).
- [14] D. Androic, et al., The G0 Experiment: Apparatus for Parity-  
 493 Violating Electron Scattering Measurements at Forward and  
 494 Backward Angles, Nucl. Instrum. Meth. A646 (2011) 59–86.  
[arXiv:1103.0761](https://arxiv.org/abs/1103.0761), doi:10.1016/j.nima.2011.04.031.
- [15] D. S. Carman, et al., The CLAS12 Forward Time-of-Flight Sys-  
 495 tem, to be published in Nucl. Inst. and Meth. A, (2020) (see this  
 496 issue).
- [16] M. Ungaro, et al., The CLAS12 Geant4 Simulation, to be pub-  
 497 lished in Nucl. Inst. and Meth. A, (2020) (see this issue).
- [17] V. Ziegler, et al., The CLAS12 Software Framework and Event  
 498 Reconstruction, to be published in Nucl. Inst. and Meth. A,  
 499 (2020) (see this issue).

**LaTeX Source Files**

[Click here to download LaTeX Source Files: cnd.tar](#)

Figure1

[Click here to download high resolution image](#)

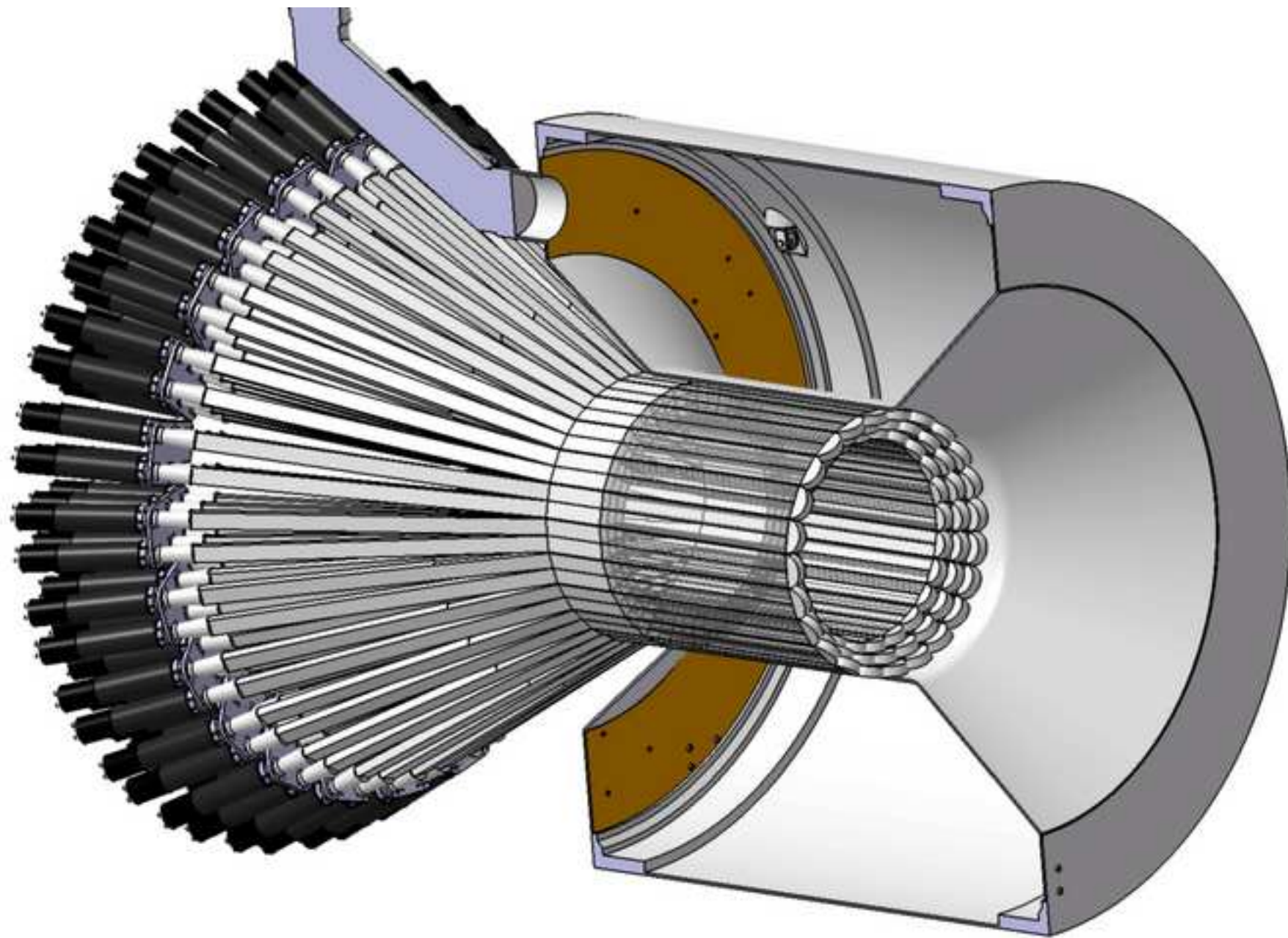


**Figure2**

[Click here to download high resolution image](#)



Figure3

[Click here to download high resolution image](#)

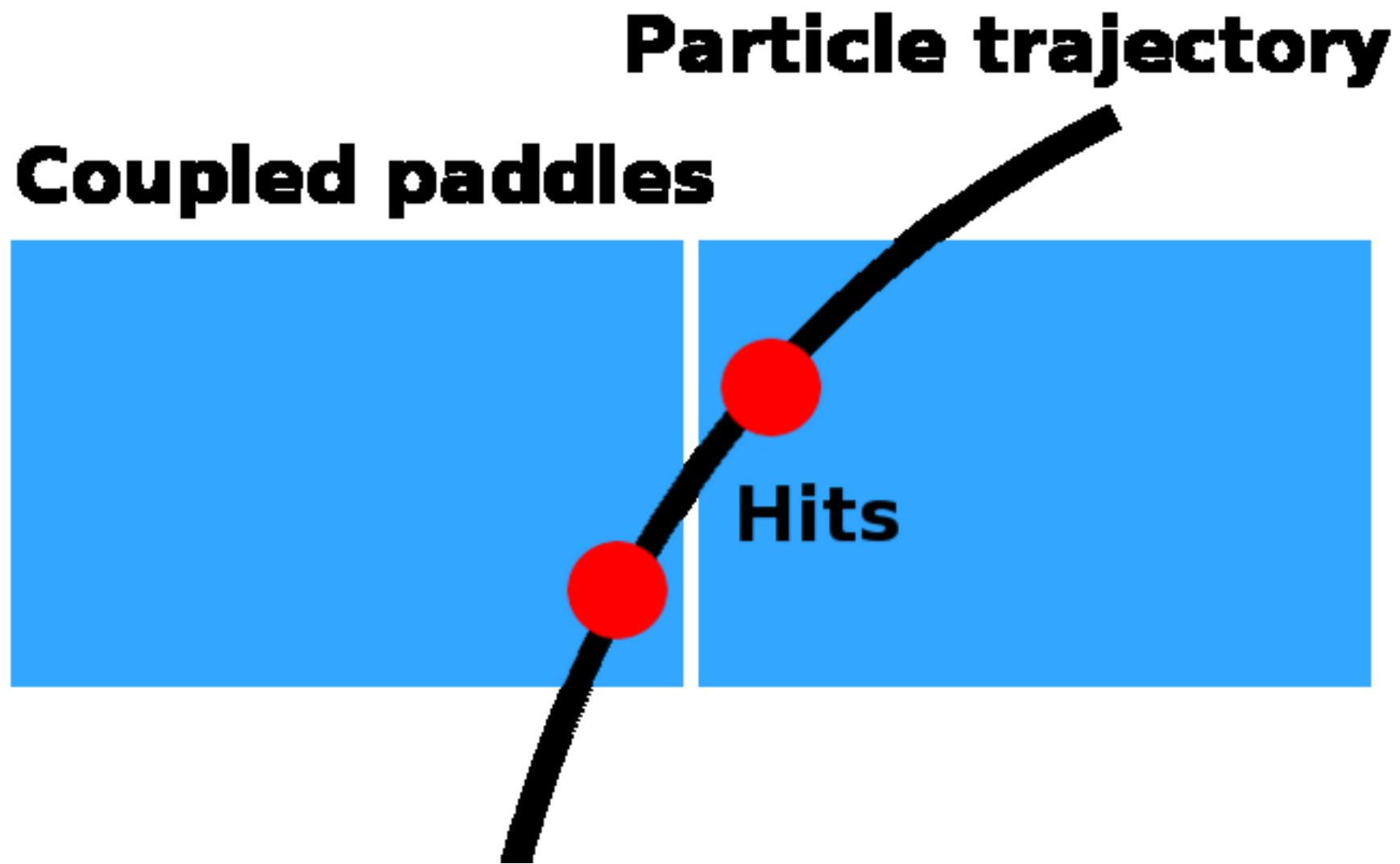


Figure4

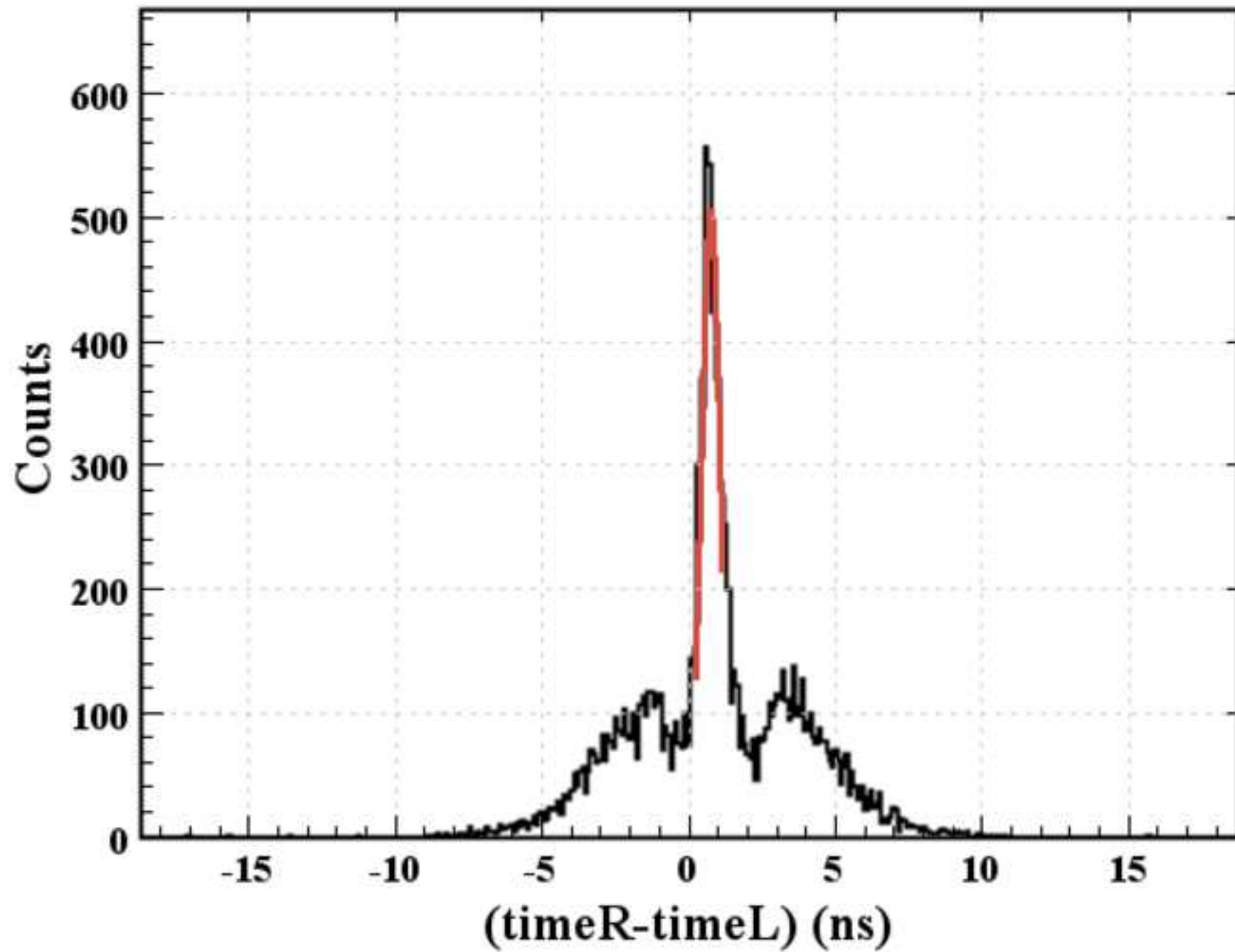
[Click here to download high resolution image](#)

Figure5

[Click here to download high resolution image](#)

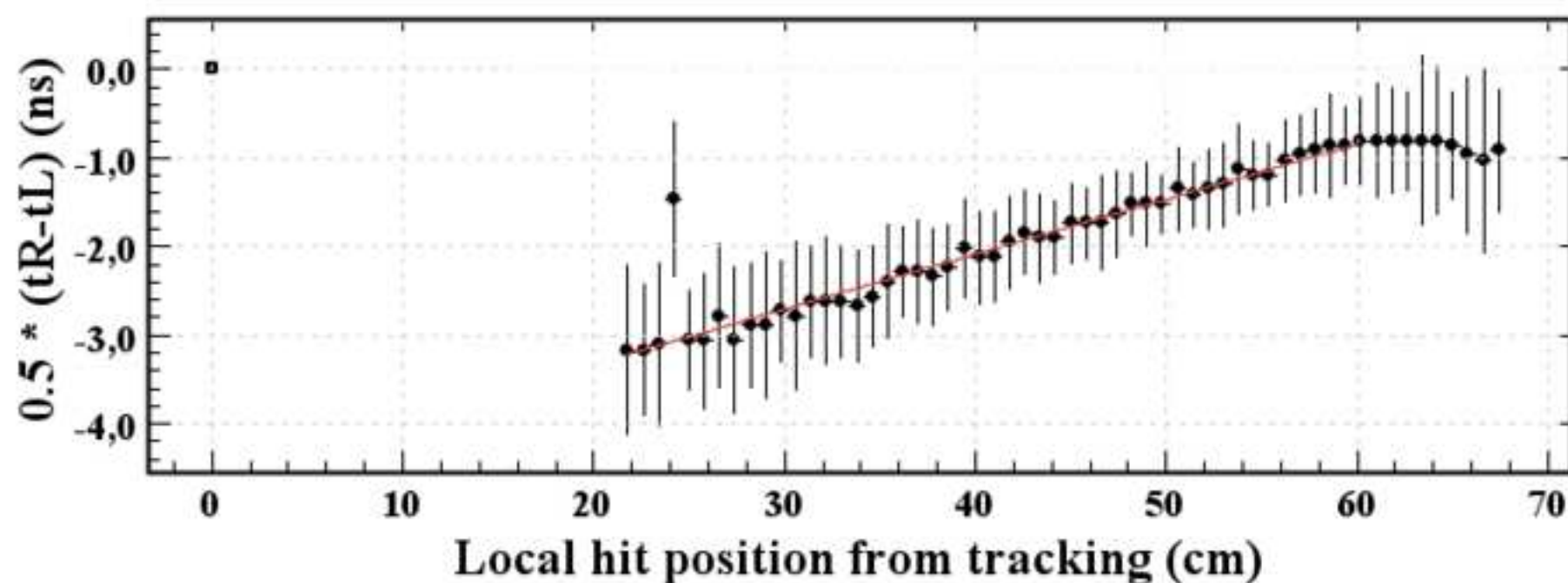
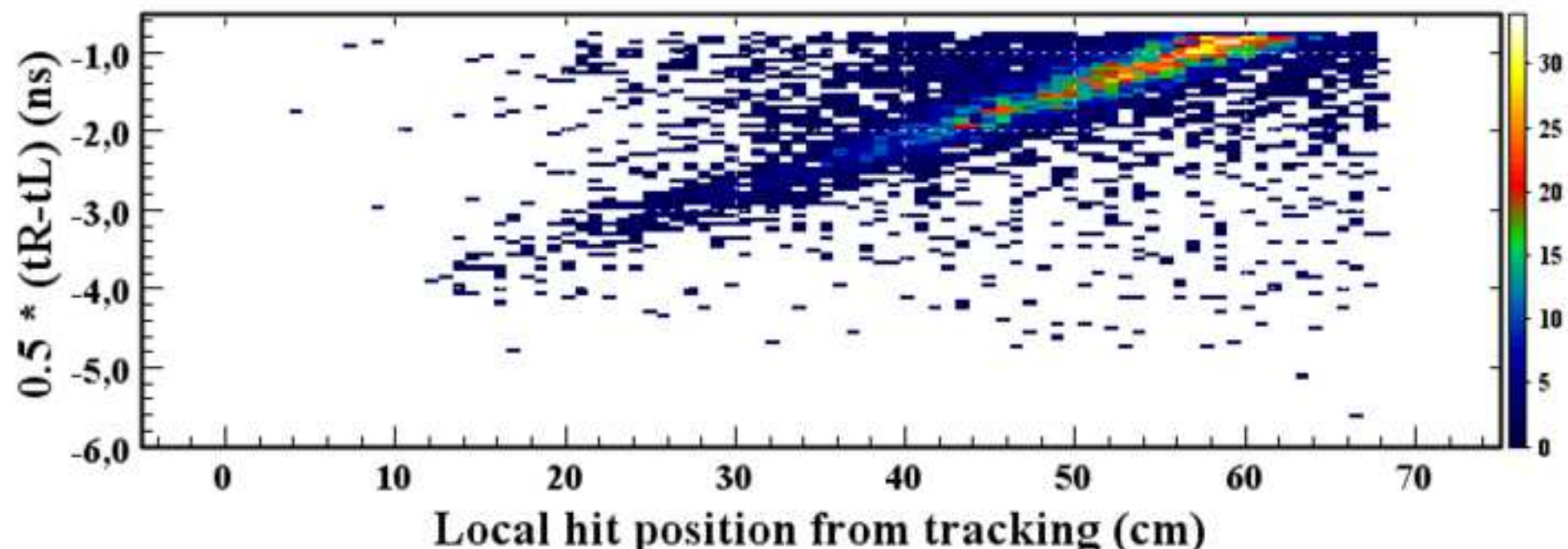


Figure6

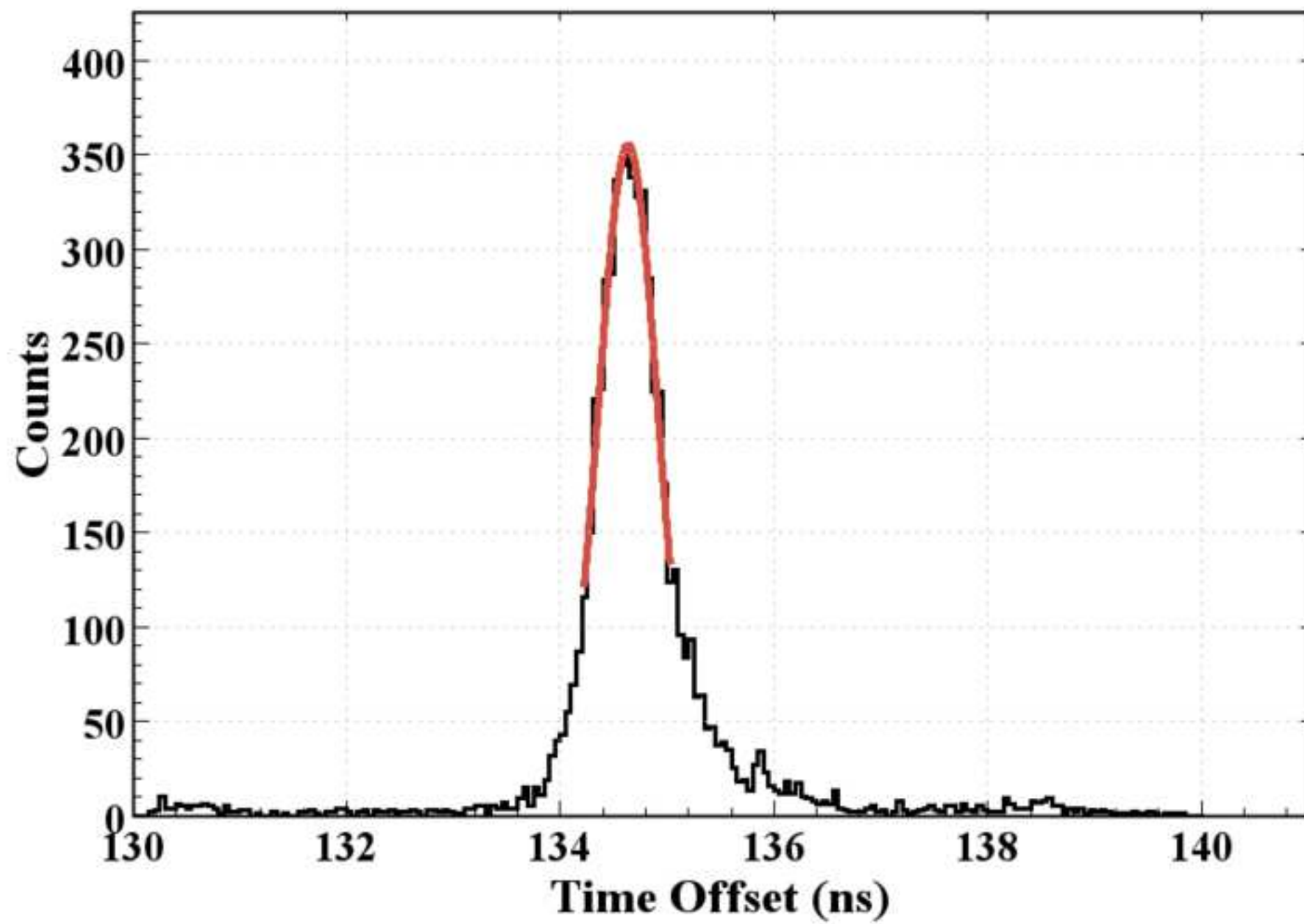
[Click here to download high resolution image](#)

Figure7

[Click here to download high resolution image](#)

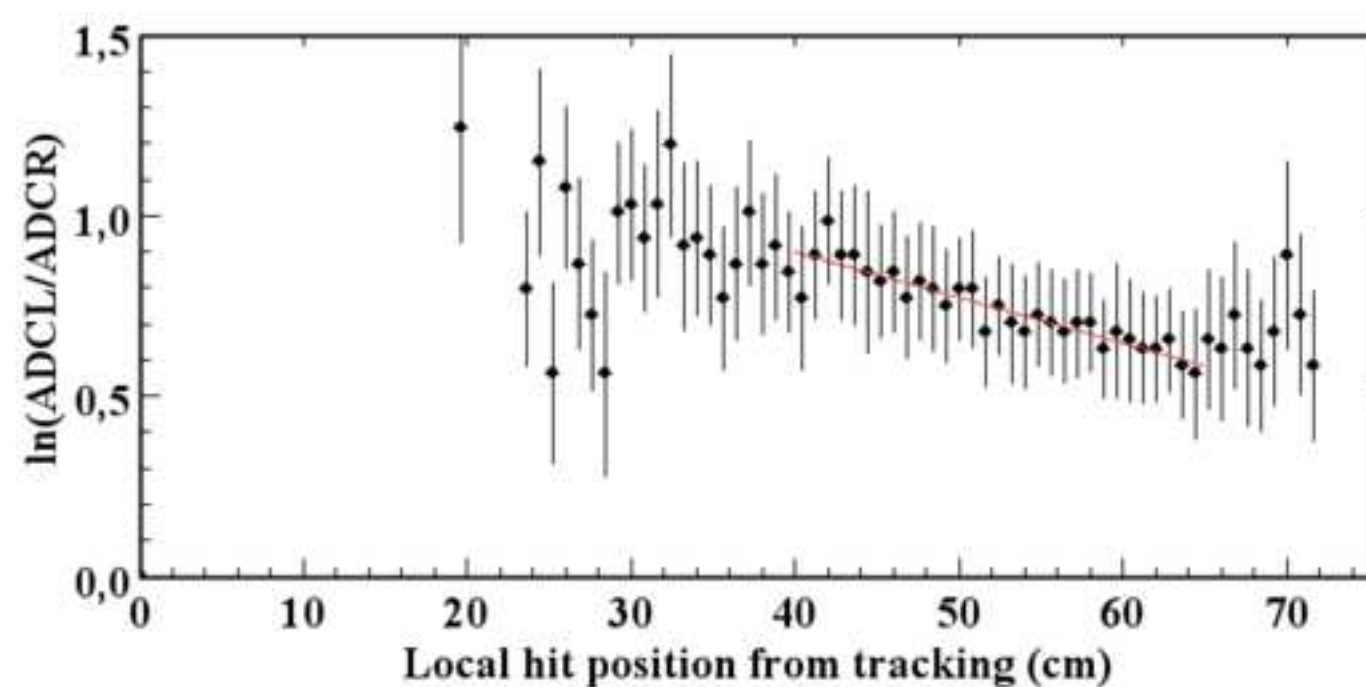
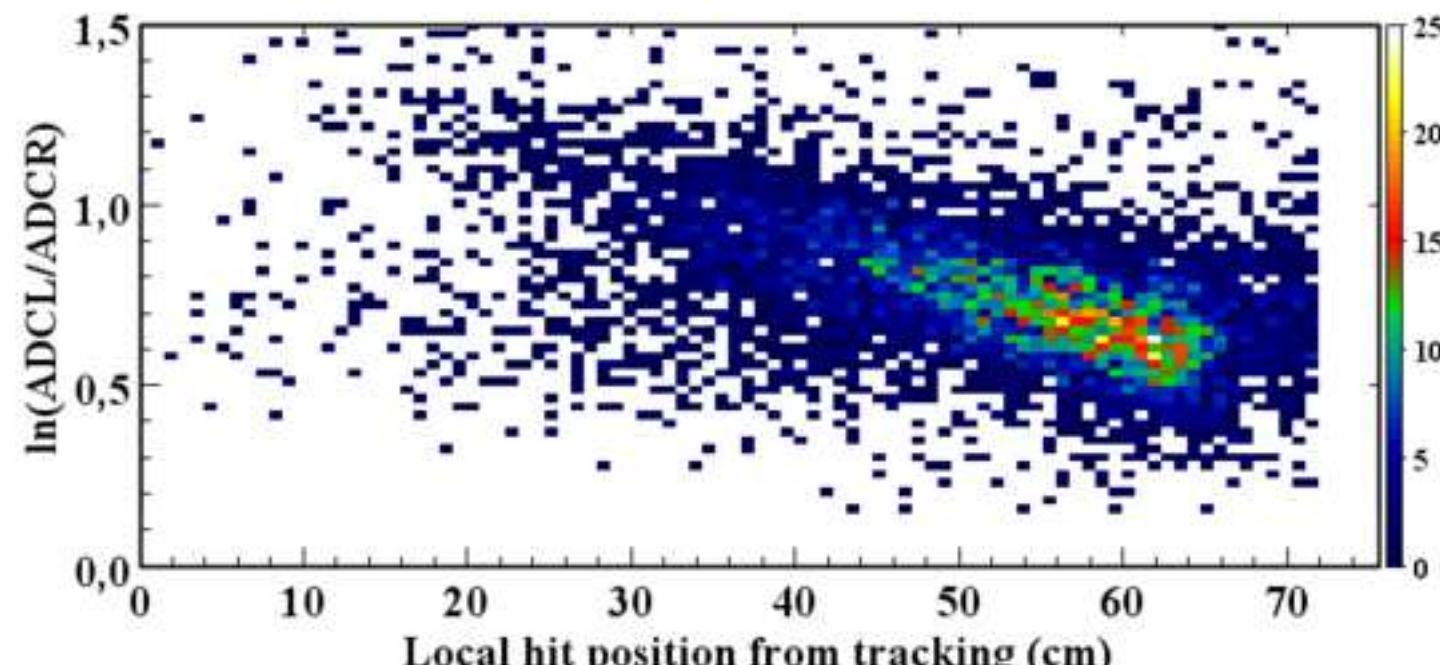


Figure8

[Click here to download high resolution image](#)